

Validation of an In Vivo Medical Image-Based Young Human Lumbar Spine Finite Element Model

Matthew J. Mills

Mechanical and Aerospace
Engineering Department,
University of California, Davis,
2132 Bainer Drive,
Davis, CA 95616
e-mail: mjmills@ucdavis.edu

Nesrin Sarigul-Klijn¹

Professor
Fellow ASME
Mechanical and Aerospace
Engineering Department,
University of California, Davis,
2132 Bainer Drive,
Davis, CA 95616;
Biomedical Engineering Department,
University of California, Davis,
451 E. Health Sciences Drive,
Davis, CA 95616
e-mail: nsarigulklijn@ucdavis.edu

Mathematical models of the human spine can be used to investigate spinal biomechanics without the difficulties, limitations, and ethical concerns associated with physical experimentation. Validation of such models is necessary to ensure that the modeled system behavior accurately represents the physics of the actual system. The goal of this work was to validate a medical image-based nonlinear lumbosacral spine finite element model of a healthy 20-yr-old female subject under physiological moments. Range of motion (ROM), facet joint forces (FJF), and intradiscal pressure (IDP) were compared with experimental values and validated finite element models from the literature. The finite element model presented in this work was in good agreement with published experimental studies and finite element models under pure moments. For applied moments of 7.5 N-m, the ROM in flexion-extension, axial rotation, and lateral bending were 39 deg, 16 deg, and 28 deg, respectively. Excellent agreement was observed between the finite element model and experimental data for IDP under pure compressive loading. The predicted FJFs were lower than those of the experimental results and validated finite element models for extension and torsion, likely due to the nondegenerate properties chosen for the intervertebral disks and morphology of the young female spine. This work is the first to validate a computational lumbar spine model of a young female subject. This model will serve as a valuable tool for predicting orthopedic spinal injuries, studying the effect of intervertebral disk replacements using advanced biomaterials, and investigating soft tissue degeneration. [DOI: 10.1115/1.4042183]

Introduction

Mathematical modeling of the human spine can be used to study spinal biomechanics while avoiding the difficulties, limitations, and ethical concerns associated with physical experimentation [1]. Such models can serve as a valuable tool for understanding how tissue degeneration, surgical procedures, artificial disk replacements, and dynamic stabilization devices affect spinal behavior [2–5]. Additionally, mathematical models can aid in the development of noninvasive medical procedures. Changes in spine morphology, material properties, applied loads, and boundary conditions can be conveniently implemented, making mathematical modeling a cost-effective alternative to physical experimentation [1]. However, validation of such models is necessary to ensure that the modeled system behavior accurately represents the physics of the actual system [6]. Validation of multisegment spine finite element (FE) models typically involves comparison of range of motion (ROM), facet joint forces (FJF), and intradiscal pressure (IDP) to experimental results [1,7]. Once validated, a model can be used to simulate a variety of loading conditions and serve as a predictive clinical tool. The objective of this work was to validate a finite element model of a young female lumbosacral spine.

Many groups have used FE models to study the biomechanics of the lumbar spine [4,5,7–22]. Breau et al. created one of the earliest lumbar spine finite element models [8]. This nonlinear, three-dimensional, L1–S1 model was based on cadaveric computed tomography (CT) scans of a 65-yr-old male subject. This work

provided a detailed procedure for generating a lumbar spine finite element model based on the medical imaging. Following the seminal work of Breau and coworkers, finite element models of the lumbar spine have been used to investigate nondegenerate [7,9–11,14,16,22,23] and degenerate [18,21] spinal biomechanics, intervertebral fusion [12], disk arthroplasty [4,17,24], and spine stabilization devices [5,15,19,20].

Shirazi-Adl performed stress analysis on the lumbar spine under torsion, sagittal, and lateral moments using the model developed by Breau [9,10]. Kong et al. investigated the biomechanics of the lumbar spine during static lifting using a lumbar spine finite element model that incorporated muscle fascicle forces [11]. The geometry of the model was based on CT scans of a 60-yr-old female cadaver. Zander et al. developed a L1–L5 lumbar spine finite element model based on geometric dimensions in the literature to predict muscle forces during upper-body inclination [14]. Eberlein et al. created a FE model of a cadaveric L2–S spine and compared the range of motion to a physical experiment. Differences between results of the FE model and the cadaveric experiment were attributed to the level of soft tissue degeneration [7]. Little et al. used a finite element model of the lumbar spine based on medical imaging from the visible human CT dataset to investigate coupled rotations due to the disks, ligaments, and facet joints [16]. Ayturk and Puttlitz developed and validated a L1–L5 finite element model from CT scans of a 49-yr-old cadaver for studying the effects of degeneration on spinal biomechanics [18]. Schmidt et al. developed a L1–L5 lumbar spine finite element model based on CT and MRI imaging of an L4–L5 motion segment to study the effect of multilevel disk arthroplasty on spine kinematics [4,24]. Park et al. used a L1–S finite element model of the lumbar spine of a 26-yr-old male subject to study the effect of disk degeneration on intersegmental rotations, intradiscal

¹Corresponding author.

Manuscript received May 5, 2018; final manuscript received November 25, 2018; published online January 18, 2019. Assoc. Editor: Joel D. Stitzel.

pressures, and facet joint forces [21]. More recently, Xu et al. developed and validated five L1–L5 lumbar spine finite element models based on CT medical imaging of male and female healthy subjects with ages ranging from 22 to 49 [22].

Finite element models of the lumbar spine can be used to improve patient care; however, the model being used must be an accurate representation of the patient's spine. Most finite element models of the lumbar spine are based on imaging of elderly cadaveric subjects [7,8,10,11,25]. Furthermore, no lumbar spine finite element models have been generated based on medical imaging from a young female subject. Female lumbar spines exhibit statistically smaller vertebral bodies, endplate diameters, intervertebral disk cross-sectional area [26–28], and greater lumbar lordosis in the standing position than male spines [29]. Moreover, aging results in both morphological and material property changes to the spine [2]. In a recent sensitivity study performed by Zander et al., lumbar spine morphology and intervertebral disk material properties were found to have the greatest influence on spinal biomechanics [30]. Given the unique morphology of the young female spine, biomechanical investigations should be performed using representative geometry, rather than models developed from elderly cadaveric subjects.

The goal of this work was to validate an in vivo medical image-based lumbar spine finite element model of a 20-yr-old living female subject under pure moments. The validation presented herein will serve as a baseline for future finite element models of the young female spine. Moreover, this work is the first step toward the development of a clinical tool for studying the intact and degenerate spine of young female patients.

Methods

Finite Element Model. The three-dimensional, nonlinear finite element model, pictured in Fig. 1, was based on in vivo CT scans of a 20-yr-old female subject with no known spinal abnormalities. Internal Review Board approval was obtained from the University of California, Davis Medical Center. The spine was scanned with a 1.25-mm slice thickness, and segmentation was performed using

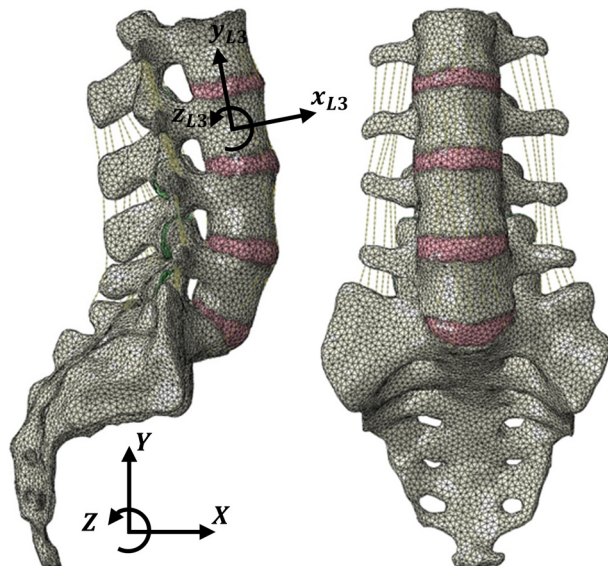


Fig. 1 Medical image-based nonlinear finite element model of the L2–S lumbosacral spine based on a living 20-yr-old female subject with no known spinal abnormalities. X—Global coordinate system anterior direction, Y—Global coordinate system superior direction, Z—Global coordinate system transverse direction, x_{L3} —L3 vertebra local coordinate system x-axis, y_{L3} —L3 vertebra local coordinate system y-axis, z_{L3} —L3 vertebra local coordinate system z-axis.

a predefined threshold values for bone. Image reconstruction was performed using mimics image processing software (MATERIALISE, v. 16.0). This high fidelity model accounted for patient-specific regional variation in bone mineral density (BMD) by converting CT Hounsfield units into density using

$$\rho = 0.047 + (1.12 \times 10^{-3}) \cdot \text{HU} \quad (1)$$

where the bone mineral density ρ has units of kilogram per cubic millimeter, and HU is the measured Hounsfield unit intensity [31]. Each vertebra was subdivided into ten intervals corresponding to BMD ranges which were used for assigning material properties for the cortical bone, cancellous bone, and posterior elements. Development of the finite element model is documented elsewhere in detail [31–35].

All seven lumbar spine ligaments were included and modeled as nonlinear axial spring elements. All ligaments except the supraspinous ligament (SSL) were modeled as tension-only springs. The SSL has been found to resist extension motion [36]; hence, it was assigned compressive properties as well. The baseline ligament stiffnesses, shown in Fig. 2, were derived from an experimental study [37]. The ligament attachment points were determined using MRI scans, known anatomical information from the literature, and input from an expert spine surgeon. Cancellous and cortical bones were modeled as linear elastic transversely isotropic, while the posterior elements were modeled as linear elastic isotropic [38–42]. The material properties used for the bony structures are presented in Table 1. The facet joint cartilage was modeled as a 0.5-mm linear elastic isotropic solid layer [43], with hard normal contact defined between adjacent cartilaginous surfaces. A surface-to-surface, finite-sliding contact formulation, with a penalty method for constraint enforcement, was used for the analyses [44]. The nucleus pulposus was modeled as an incompressible hyperelastic solid using a *Mooney–Rivlin model* [45]. Finally, the annulus fibrosus was modeled as a continuous distribution of two fiber populations embedded in an isotropic ground substance, using continuum theory for fiber-reinforced composites originally developed by Spencer [46]. It was assumed that collagen fiber stiffness was constant throughout the AF and was therefore derived by taking the average fiber stiffness from the radial and circumferential regions of the AF [47]. It is well known that fiber angles vary from approximately ± 23 deg to ± 47 deg moving circumferentially from an anterior to a posterior location [47]. Therefore, average fiber inclinations of ± 30 deg relative to horizontal were assumed. The material properties used for the soft tissues are presented in Table 2 and the constitutive equations for soft tissue material models have been presented in the Appendix. Since the finite element model was generated from CT scans of a living patient, determination of material properties through experimentation was not possible. Thus, material properties were derived from experimental studies available in the literature. Material properties specific to the young female spine are not

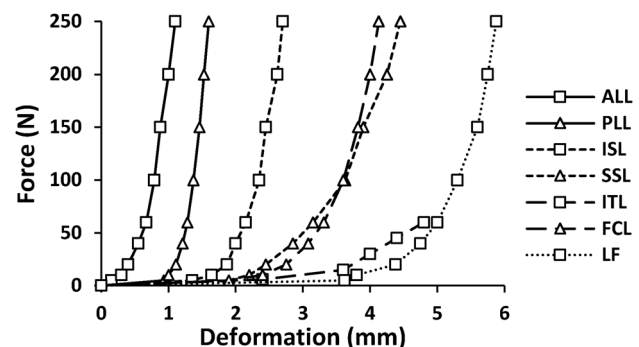


Fig. 2 Calibrated ligament stiffness curves: ALL, PLL, ISL, SSL, intertransverse ligament, facet capsular ligament, and LF

Table 1 Material properties for bony structures in lumbar spine finite element model [38–42]

Structure	Young's modulus, E (MPa)	Shear modulus, G (MPa)	Poisson's ratio, ν
Cancellous bone ^a	$E_{xx} = 140$	$G_{xy} = 48.3$	$\nu_{xy} = 0.450$
	$E_{yy} = 140$	$G_{xz} = 48.3$	$\nu_{xz} = 0.315$
	$E_{zz} = 200$	$G_{yz} = 48.3$	$\nu_{yz} = 0.315$
Cortical bone ^a	$E_{xx} = 11,300$	$G_{xy} = 3800$	$\nu_{xy} = 0.484$
	$E_{yy} = 11,300$	$G_{xz} = 5400$	$\nu_{xz} = 0.203$
	$E_{zz} = 22,000$	$G_{yz} = 5400$	$\nu_{yz} = 0.203$
Posterior elements	$E = 3500$	$G = 1400$	$\nu = 0.250$

^ax-direction: lateral, y-direction: anterior/posterior, and z-direction: superior/inferior.

Note: E_{ii} —Young's modulus in the i -direction, G_{ij} —shear modulus in j -direction with surface normal in the i -direction, and ν_{ij} —Poisson's ratio corresponding to a contraction in the j -direction for a given extension in the i -direction.

Table 2 Material properties for lumbar spine soft tissues

Structure	Ground substance	Fibers	Source
Nucleus pulposus	$C_{10} = 0.12$ $C_{01} = 0.03$	N/A	[31]
Annulus fibrosus	$C_{10} = 0.250$	$k_1 = 3.0$ MPa $k_2 = 45$ $\phi_1 = 30$ deg $\phi_2 = -30$ deg	[61]
Facet cartilage	$E = 35.0$ MPa $\nu = 0.4$	N/A	[4]

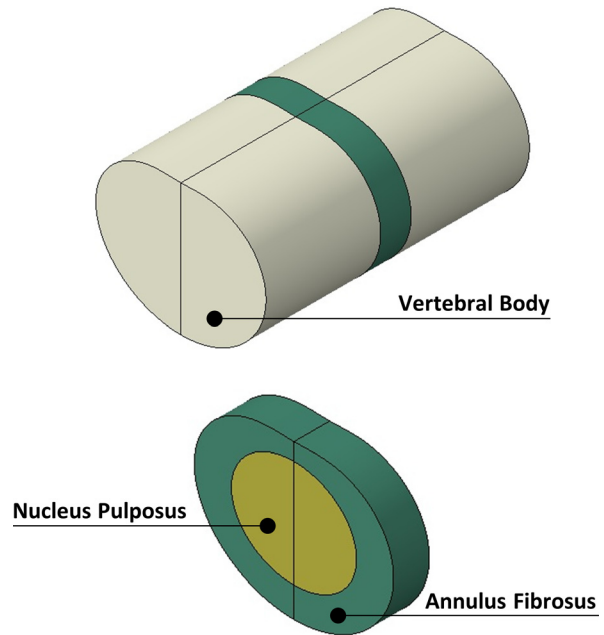
Note: C_{10} , C_{01} —Mooney–Rivlin material model constants, k_1 , k_2 —Material properties of the fibers, ϕ_1 , ϕ_2 —inclination of fiber population relative to horizontal, E —Young's modulus, and ν —Poisson's ratio.

readily available; therefore, care was taken to use material properties from healthy specimens with minimal degeneration.

To simulate flexion–extension, lateral bending and axial rotation, pure moments were applied to the cranial surface of the L2 vertebra in each of the three global anatomical directions (i.e., anterior–posterior, inferior–superior, transverse), while the sacrum was fixed in all degrees-of-freedom. The applied moments were unconstrained; therefore, they followed the motion of the L2 vertebra. A local coordinate system was fixed to each vertebra for the purpose of measuring intervertebral rotations. Both the local and global coordinate systems have been depicted in Fig. 1. Note that forces due to body weight and musculature were not considered in this work; hence, a follower load was not incorporated in the model [48]. Static analyses were performed with large displacement theory using the ABAQUS/STANDARD v6.12-1 FEA solver (Dassault Systèmes Simulia Corp., Providence, RI) on a workstation with two Intel® Xeon® 2.3 GHz CPUs with 128 GB RAM on 22 cores. The geometry was meshed using solid tetrahedral elements.

Convergence Study. A convergence study was performed by applying pure flexion and axial rotation moments to a simplified L3–L4 spinal segment depicted in Fig. 3. Using a simplified model for the convergence study that accurately represented the true geometry allowed for reduced computation time while providing an accurate indication of the convergence trend. Analytic representation of the intervertebral disk geometry was obtained by fitting the parameterization proposed by Korez et al. to the true dimensions of the L3–L4 disk [49]. The parametrization, which assumes an ellipse modified by Gaussian functions at specific anatomical locations, is given by

$$r(\theta) = \frac{A \cdot B}{\sqrt{(A \sin \theta)^2 + (B \cos \theta)^2}} \cdot \left[1 + \sum_{i \in \{l, r, f, a\}} m_i \exp \left(-\frac{(\theta - \varphi_i)^2}{2\sigma_i^2} \right) \right] \quad (2)$$

**Fig. 3 Simplified L3–L4 vertebral motion segment model used for convergence study**

where A and B are the semimajor and semiminor axes, m is the magnitude of the Gaussian function, φ_i is the angular position that the Gaussian function is centered, σ_i is the standard deviation of the Gaussian function, and l, r, f , and a stand for the left pedicle, right pedicle, vertebral foramen, and anterior part of the vertebral body, respectively.

The L3 and L4 vertebral bodies were extruded from the simplified intervertebral disk at the appropriate distance to represent the true vertebral geometry. Since bone is significantly stiffer than the intervertebral disk, the internal strain energy of spine is insensitive to the bone material properties [30]. Therefore, it was assumed that the vertebrae consisted of only cancellous bone. Additionally, the small intervertebral angle was neglected.

Seven tetrahedral mesh seed lengths from 5 to 1.5 mm and two element orders (linear, quadratic) were used for the convergence study. The caudal surface of the L3 vertebra was fixed in all degrees-of-freedom, while a pure moment of 7.5 N·m was applied to the cranial surface of the L4 vertebra [50]. The internal strain energy was taken as the field variable of interest as it provides a measure of the solution in the whole domain. H-convergence was assessed by evaluating the change in internal strain energy between the mesh seed sizes, using both linear and quadratic elements. Additionally, p -convergence was assessed by evaluating

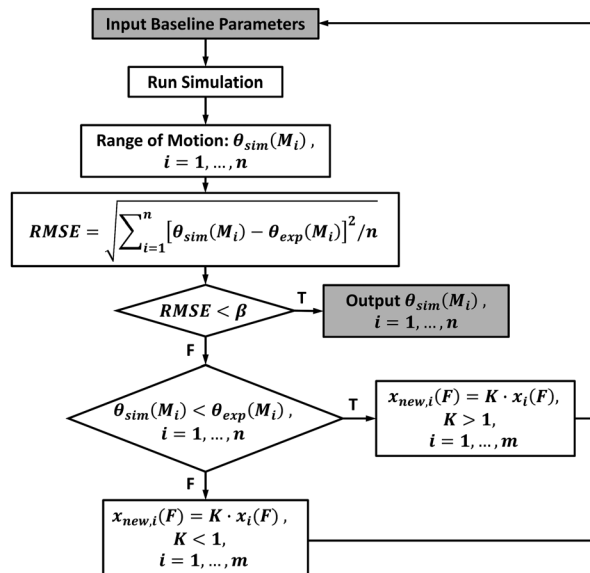


Fig. 4 Ligament calibration algorithm: $\theta_{sim}(M_i)$ —computed ROM, $\theta_{exp}(M_i)$ —experimental ROM, M_i — i th moment, n —number of data points, β —threshold value, $F_i(x)$ —initial ligament load–displacement function, $F_{new,i}(x)$ —adjusted ligament load–displacement function, k —displacement scaling factor, and m —number of active ligaments

the change in internal strain energy resulting from a change of element order for the same mesh size. A convergence criterion of $\pm 5\%$ change was used for both h - and p -convergence [6,18].

Ligament Calibration. There is significant uncertainty associated with spinal ligament material properties due to difficulties associated with harvesting and testing samples. This material property uncertainty, coupled with ligament modeling uncertainties (i.e., the use of discrete, nonlinear spring elements) can lead to inaccurate simulation results. Therefore, a calibration algorithm was used to adjust the baseline ligament stiffness curves to obtain physiological ranges of motion [37]. The algorithm, shown schematically in Fig. 4, adjusted the ligament force–displacement curves through a displacement scaling factor if the root-mean-square error (RMSE) was above a threshold value β . If the computed range of motion θ_{sim} was too stiff as compared to experimental data θ_{exp} , the active ligaments' force–displacement curves were multiplied by a displacement scaling factor K greater than unity. Conversely, if the computed range of motion was too flexible, the active ligaments' force–displacement curves were multiplied by a displacement scaling factor K less than unity. Note that the term *active ligaments* refer to ligaments that have a significant influence on the range of motion in a particular loading modality. The influence of each lumbar ligament on the range of motion under pure moments has been determined experimentally through stepwise resection of spinal structures [36]. For instance, the active ligaments for flexion are the ligamentum flavum (LF), posterior longitudinal (PLL), interspinous (ISL), and supraspinous ligaments. For extension, the active ligament is the anterior longitudinal ligament (ALL). Note that the torsion and lateral bending ranges of motion were well within experimental ranges; therefore, calibration was only performed for motion in the sagittal plane.

Results

The results of the h - and p -convergence are presented graphically in Fig. 5 for both linear and quadratic tetrahedral elements. For all mesh sizes, changing the element order from linear to quadratic had a significant influence on the internal energy in the

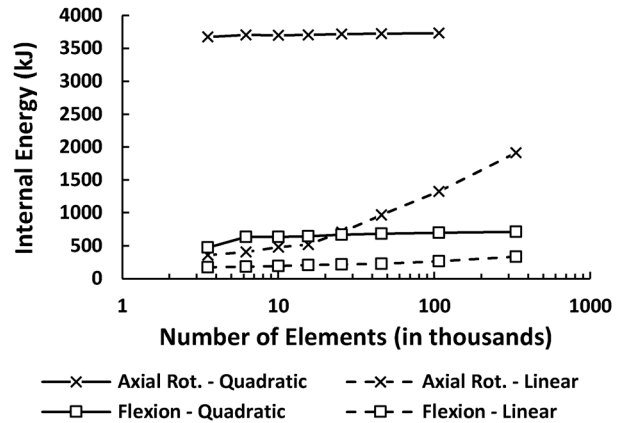


Fig. 5 Convergence study results for applied moments of 7.5 N-m in flexion and axial rotation

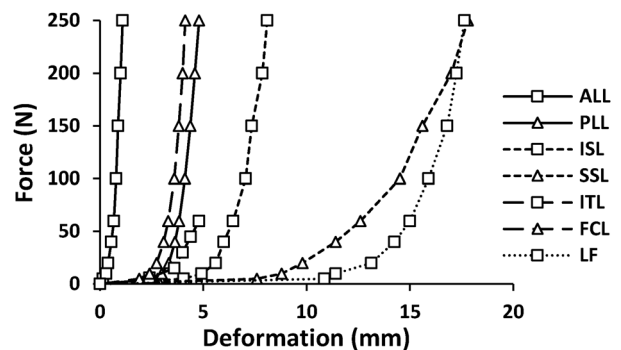


Fig. 6 Calibrated ligament stiffness curves: ALL, PLL, ISL, SSL, intertransverse ligament, facet capsular ligament, and LF

system. The linear element analyses did not reach an asymptotic solution and had significant percent change between mesh densities. This result was expected as linear tetrahedral elements are not well suited for biomechanical finite element simulations [51]. Conversely, the quadratic element analyses exhibited an upward asymptotic trend with a percent change of internal energy for mesh densities smaller than 4-mm being less than 5%. Interestingly, the internal energy was more sensitive to the mesh size for flexion loading than torsional loading. Based on the results of the p -convergence study, quadratic tetrahedral elements were used for the lumbar spine simulations. A mesh density of 3-mm was chosen to yield an accurate solution while maintaining an acceptable computation time.

The calibrated ligament load–displacement curves are presented in Fig. 6. The chosen threshold RMSE β was 0.70 radians, and was computed based on the mean lumbar range of motion curve from experimental in vitro results [52]. The selected value for β yielded physiological motion similar to known experimental data.

Total ranges of motion for applied moments of 7.5 N-m are presented in Fig. 7. The total range of motion in flexion–extension, axial rotation and lateral bending were 39 deg, 16 deg and 28 deg, respectively. The total range of motion for flexion–extension, axial rotation, and lateral bending were comparable to the experimental findings and validated finite element models, as shown in Fig. 7 [1,7,52]. The flexion–extension range of motion was slightly above the range of results found by Rohlmann et al. but was within the range of finite element models presented in the work by Dreischarf et al. [1]. The lateral bending range of motion was within the ranges for the Rohlmann experimental study and the finite element models in the literature. The axial rotation range

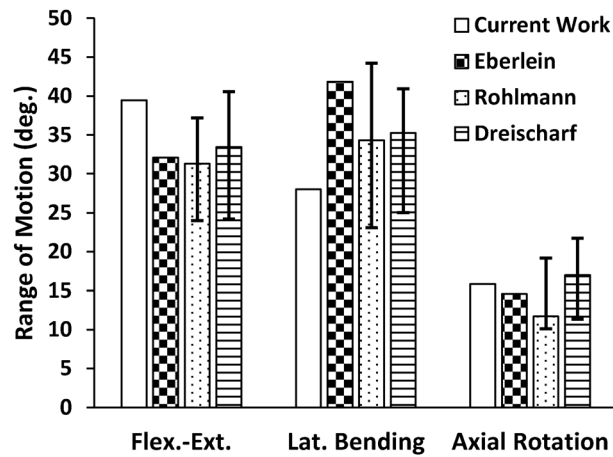


Fig. 7 Total L2-S ROM for 7.5 N-m applied moments compared with in vitro experimental studies and validated FE models. The first bar shows the results for the finite element model presented in this work. The second bar shows the results from a L2-S in vitro study of a single specimen [7]. The third bar indicates the median and range of results for the motion for ten L5-L1 specimens [52]. The fourth bar shows the median ROM values of eight validated finite element models and their range of results [1].

of motion was in excellent agreement with both the experimental studies and finite element models. The difference between the total range of motion in this work and the median range of motion from the Rohlman et al. experimental study were 8.2 deg, -6.28 deg, and 4.12 deg in flexion-extension, axial rotation, and lateral bending, respectively.

Rotation angles for the whole lumbosacral spine were plotted versus the applied moment in Fig. 8. The maximum flexion range of motion under 10 N-m was 24 deg, whereas the maximum extension range of motion was 21 deg, yielding a total range of motion of 45 deg. Maximum total range of motion for axial rotation and lateral bending were 19 deg and 34 deg, respectively. All three range of motion curves demonstrated nonlinear stiffening as the magnitude of the applied moment was increased. The flexion-extension motion exhibited the most nonlinearity, while the axial rotation and lateral bending motion exhibited less stiffening for increased moments. The flexion L2-S load-deflection curve, shown in Fig. 8, passed through the experimental range of the Rohlmann study at 7.5 N-m and showed slightly less curvature than both the Rohlmann and Eberlein curves. The extension L2-S load-deflection curve was in good agreement with experimental studies but exhibited a slightly more flexible response. The flexion response was more flexible than the extension response, which aligns with experimental observations [53]. The axial rotation load-deflection curve exhibited excellent agreement with the experimental studies, passing through the experimental range of the Rohlmann study at ± 7.5 N-m with similar curvature as the experimental curves. The lateral bending curve was within the Rohlmann study ranges; however, the response had less curvature than the experimental results. The RMSE computed based on the mean lumbar range of motion curve, in radians, from the Rohlmann et al. experimental in vitro results were 0.260, 0.646, 0.061, and 0.681 in flexion, extension, torsion, and lateral bending, respectively.

The intervertebral rotations were also plotted versus applied moment as shown in Figs. 9–11. With the exception of the L5-S segment, the extension motion was stiffer than the flexion motion for all segments. For the L5-S level, both flexion and extension had similar stiffnesses. The maximum intervertebral range of motion in flexion was 6.9 deg at the L4-L5 segment. Under extension, the L3-L4, L4-L5, and L5-S levels all had a maximum range of motion of approximately 5.5 deg. The range of motion of

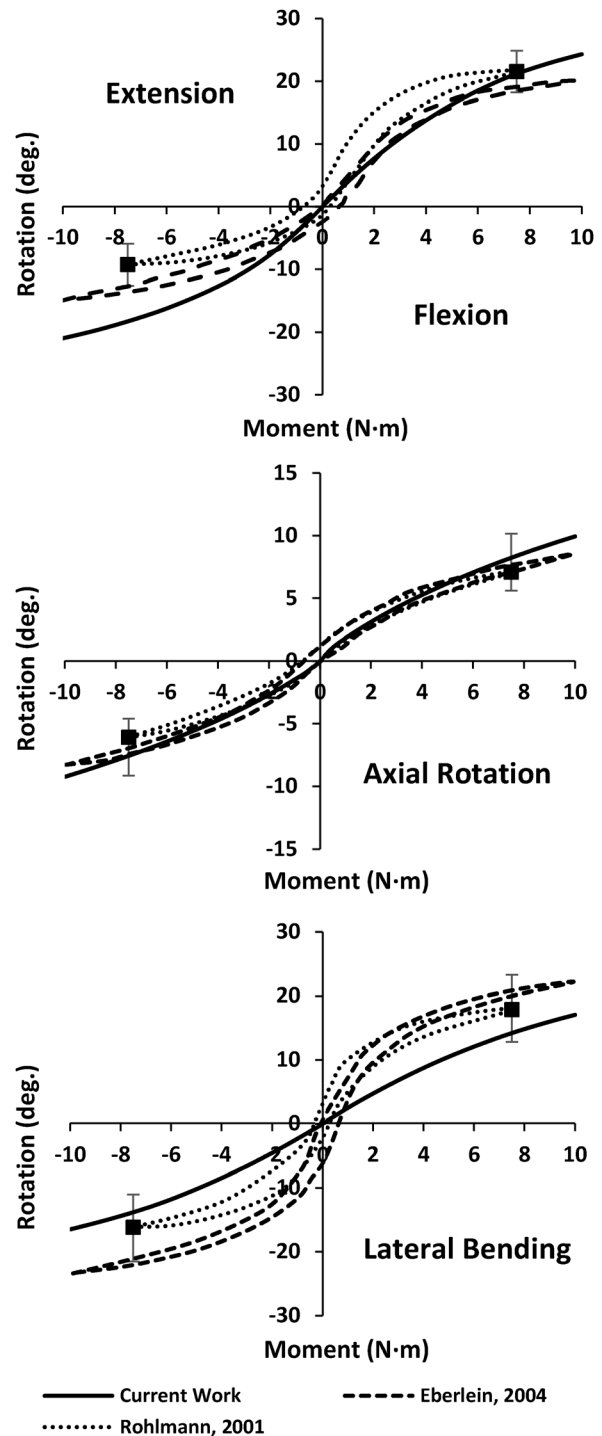


Fig. 8 Flexion-extension (top), axial rotation (middle), and lateral bending (bottom) ROM for the L2-S segment compared with in vitro experimental studies [7,52]. Error bars indicate the range of the Rohlmann experimental results at an applied moment of 7.5 N-m.

the L2-L3 segment was slightly less at 4.1 deg. The maximum intervertebral range of motion in axial rotation was 2.9 deg at the L3-L4 segment. The maximum intervertebral range of motion in lateral bending was 5.1 deg at the L3-L4 segment. For axial rotation and lateral bending, the range of motion for the L5-S segment was significantly less than all other segments. The intervertebral rotations were compared with the experimental study by Panjabi et al. [54]. Overall, good agreement was observed between the

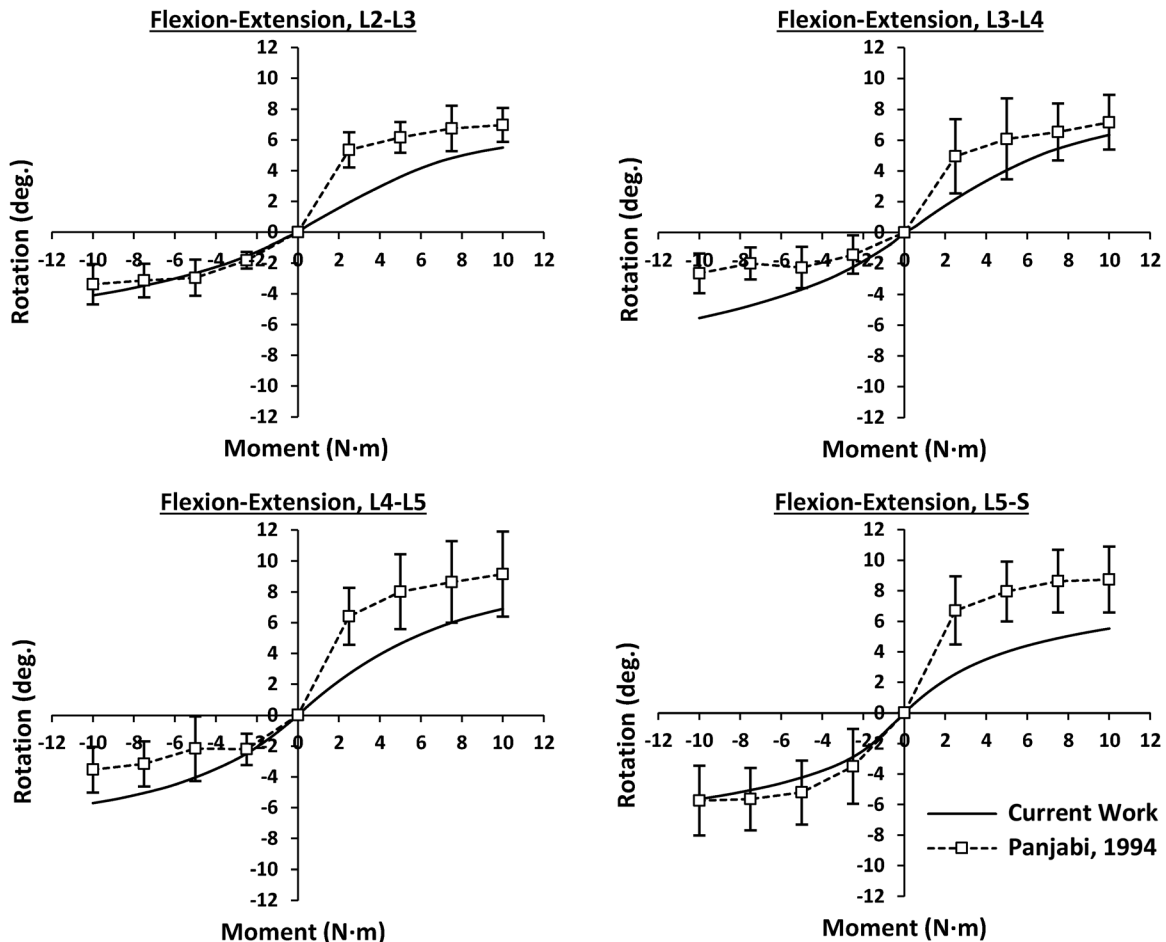


Fig. 9 Intervertebral rotations for flexion (positive) and extension (negative) compared with experimental data [54]. The experimental data points represent the mean and standard deviation of nine L1-S specimens.

finite element model and the experimental study. The L3-L4 and L4-L5 segments were more flexible in extension, and all levels were slightly stiffer than the experimental results in flexion. In lateral bending, the finite element model results exhibited less curvature than the experimental results. Also, the L5-S level was stiffer than the experimental results. The axial rotation intervertebral motion curves for the L2-L3 and L3-L4 levels were in good agreement with the experiment results. More flexible responses were predicted for the L4-L5 and L5-S spinal levels. The RMSE with respect to experimental results of Panjabi et al. are shown in Table 3 for each loading direction and spine level.

The intradiscal pressure within the nucleus pulposus versus compressive load for the L4-L5 intervertebral disk is presented in Fig. 12, and exhibited a linear relationship. Under pure compressive loads of 300 N and 1000 N, the intradiscal pressure within the nucleus pulposus of the L4-L5 intervertebral disk was 333 kPa and 933 kPa, respectively. Intradiscal pressure resulting from applied flexion moments is shown in Fig. 13. For an applied moment of 3.0 N-m, the mean intradiscal pressure in the L2-L3 and L3-L4 nuclei pulposi was 176 kPa and 101 kPa, respectively. Additionally, for an applied moment of 7.5 N-m, the mean intradiscal pressure in the L4-L5 nucleus pulposus was 270 kPa. The intradiscal pressure of the L4-L5 segment under pure compression resulted in a linear trend with respect to the magnitude of the compressive load. The results were in excellent agreement with the experimental study by Brinckmann and Grootenboer and the finite element model by Xu et al. [22,55]. The percent difference between the finite element model and the experimentally

determined intradiscal pressure by Brinckmann et al. for an applied load of 1000 N was -1.61%. Intradiscal pressure under flexion was also compared against the literature values, as shown in Fig. 13. The finite element model predicted intradiscal pressures that were similar to the experimental study and validated finite element model. The percent differences with respect to the mean intradiscal pressure from the Ayturk experimental study were -38.5%, 52.8%, and 56.1% for the L2-L3, L3-L4, and L4-L5 spine levels, respectively.

As presented in Fig. 14, the median facet joint forces for all spinal levels under 7.5 N-m applied moments were 9.1 N, 21.9 N, and 7.7 N for extension, axial rotation, and lateral bending, respectively. Facet joint forces during flexion were negligible and therefore were not presented. The facet joint forces at each lumbar spine level under 7.5 N-m applied moments are shown in Fig. 15. Under extension, the peak facet joint force was 11.9 N occurring at the L5-S level. Under axial rotation, the peak facet joint force of 32.2 N occurred at the L4-L5 level. Finally, under lateral bending the peak facet joint force of 15.5 N occurred at the L3-L4 level. The facet joint forces were compared with experimental data and finite element models in the literature under an applied moment of 7.5 N-m, as presented in Figs. 14 and 15. Under lateral bending at the L2-L3 and L4-L5 levels, the facet joint forces were in good agreement with other validated finite element models in the literature. However, under extension and axial rotation, the facet joint forces were significantly less than the experimental data and the other validated finite element models. The small facet joint forces in extension and torsion were likely a consequence of the material properties chosen for the intervertebral disks. The

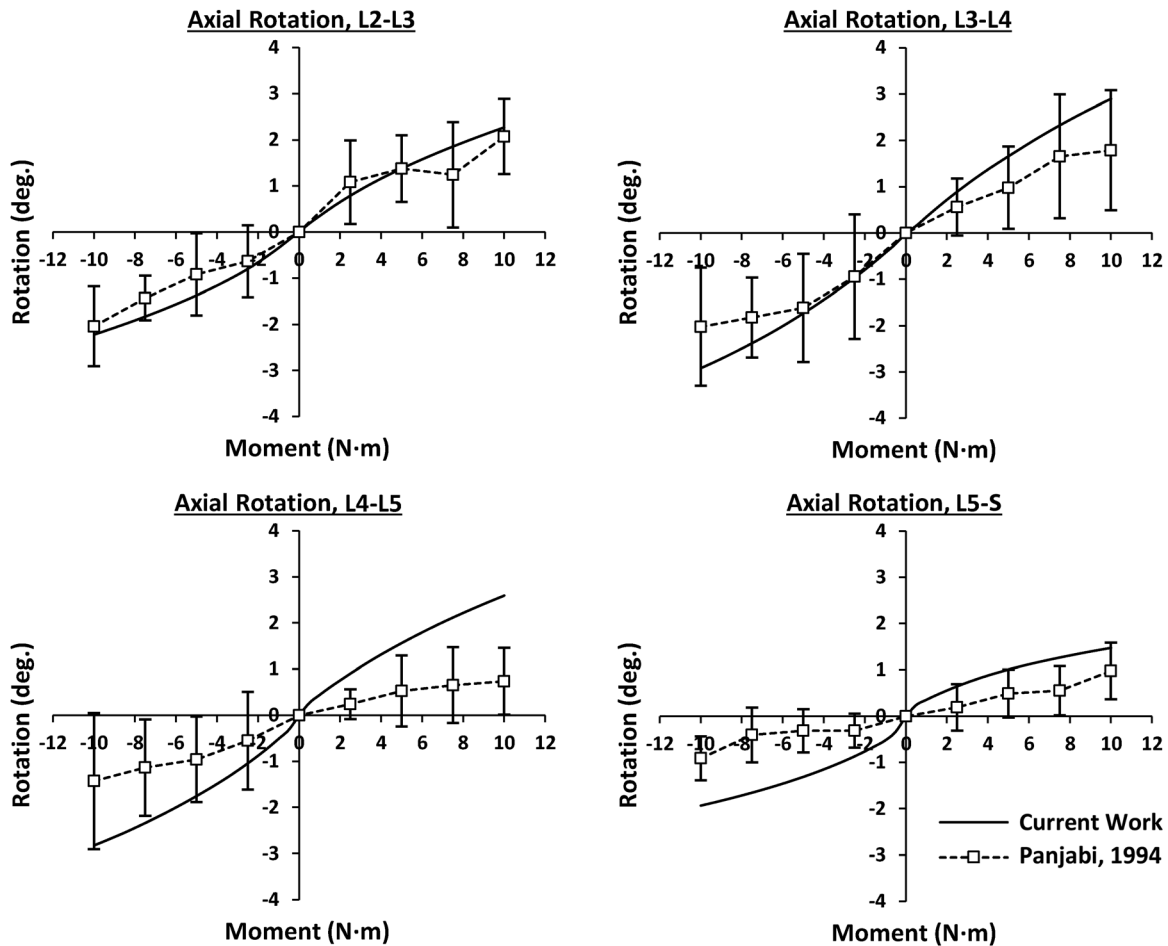


Fig. 10 Intervertebral rotations for left (positive) and right (negative) axial rotation compared with experimental data [54]. The experimental data points represent the mean and standard deviation of nine L1-S specimens.

percent differences computed from the Dresicharf finite element study were -111.3% , -119.6% , and -43.1% for extension, axial rotation, and lateral bending, respectively [1].

Discussion

The lumbar spine range of motion has a significant dependency on morphology and soft tissue material properties [30,37]. Due to the relatively flat slope of the ligament force–displacement curves for small displacements, the material properties of the intervertebral disks have a significant influence on the intervertebral rotations for small angles. For larger angles, the ligaments have more influence on range of motion resulting from their exponential force–displacement curves. Due to material property and modeling uncertainties, calibration of ligament properties was necessary to achieve physiological results from the finite element model [30,37]. There is significantly more data available on the material properties and geometric structure of the intervertebral disk; therefore, no calibration was performed for the annulus fibrosus and nucleus pulposus [47,56–58]. The intervertebral disk material properties were based on nondegenerate test data [47]; however, these structures undergo significant degeneration with aging, which has a strong influence on intervertebral rotations. Mildly degenerated disks exhibit an increase in intervertebral rotations, while a severely degenerated disk results in reduced intervertebral rotations [2]. The inclusion of tissue degeneration effects was beyond the scope of this work; however, improved agreement with the literature results could be obtained by modifying morphology and tissue degeneration to reflect the level of degeneration in the experimental in vitro studies.

Nondegenerate annulus fibrosus and nucleus pulposus material properties were used in the simulations, as previously noted. In the experimental study by Wilson et al., the average age of the cadaveric spine specimens was 76; therefore, they likely had a significant degree of degeneration [59]. It has been reported that disk degeneration leads to increased facet joint forces [2]. In this work, the primary load path occurred through the intervertebral disks due to the high stiffness associated with the chosen material properties, resulting in minimal load transfer through the posterior elements. However, if tissue degeneration had been incorporated in the annulus fibrosus and nucleus pulposus material properties, the load transfer through the facet joints would increase showing better agreement with the experimental data. Furthermore, none of the validated finite element models used for comparing the facet joint forces were generated based on the morphology of a young female subject, as was done in this work. Morphology can have a significant influence on the range of motion and facet joint forces of lumbar spine finite element models [30].

Overall, the biomechanical response of the developed lumbosacral finite element model was consistent with the published experimental data and computational models. Differences between the presented finite element model and the validation data were expected due to the unique morphology and nondegenerate material properties of a young female spine. The most notable differences were an increased stiffness in extension, increased flexibility in lateral bending, and reduced facet joint forces. The results presented herein will serve as a baseline for future finite element models of the young female spine.

The finite element model presented in this work will become a predictive clinical tool for improving patient care. Moreover, it is

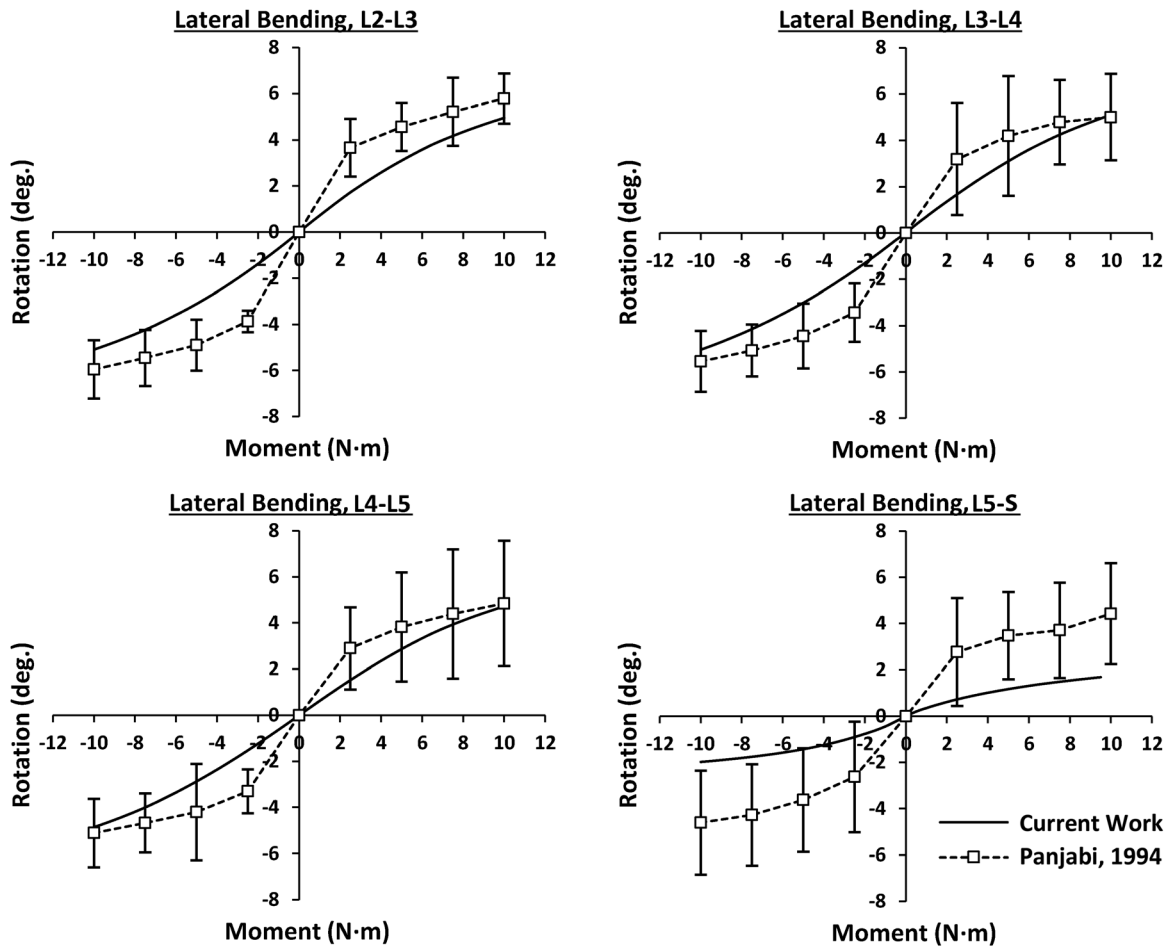


Fig. 11 Intervertebral rotations for right (positive) and left (negative) lateral bending compared with experimental data [54]. The experimental data points represent the mean and standard deviation of nine L1-S specimens.

Table 3 Intervertebral rotation RMSE with respect to experimental data [54]

Spine level	Flexion	Extension	Lateral bending	Axial rotation
L2–L3	0.086	0.016	0.074	0.017
L3–L4	0.065	0.075	0.056	0.032
L4–L5	0.107	0.060	0.051	0.059
L5–S	0.132	0.023	0.114	0.040

Note: Units: radians.

the only computational lumbar spine model based on in vivo medical imaging of a healthy, young female subject. Nonetheless, this study has several limitations that will be addressed in future work. The finite element model in this work was for a L2-S lumbar spine; however, L1–L5 lumbar spine in vitro experimental studies and finite element models were used for comparing results. Most of the published experimental work and validated finite element models are for L1–L5 geometry. It was speculated by the authors that this is a valid means of comparison since the number of intervertebral joints is the same between the two spine segments. However, validation studies should ideally be conducted with experimental studies and simulations that have the same geometry. The effect of soft tissue degeneration was not included in this study, contributing to differences between published results and the current work. Future studies will incorporate the morphology and material property changes associated with soft tissue degeneration. Finally, spinal ligaments are thin composites with a similar

histological structure as the annulus fibrosus; however, in this work they were modeled as simplified nonlinear axial springs. The accuracy of the ligament model could be improved by using continuum theory for fiber-reinforced composites, as was done for the annulus fibrosus [7]. Within such a framework, ligament geometry could be obtained from medical imaging to further improve the ligament model realism. A high fidelity ligament model with geometric dimensions extracted from in vivo medical imaging may eliminate the need to perform calibration as is typically done for lumbar spine finite element models.

Conclusion

The L2-S nonlinear finite element model presented in this work was in good agreement with published experimental in vitro studies and validated finite element models under pure moments applied to the cranial surface of the L2 vertebra. For applied

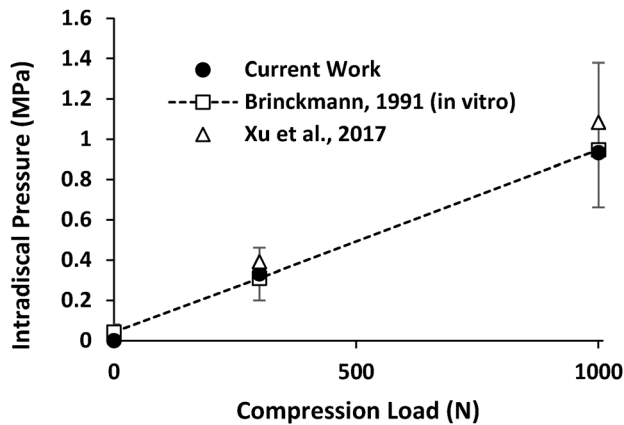


Fig. 12 IDP within the L4–L5 nucleus pulposus under compressive loading compared with experiment data [55] and a validated finite element model [22]. Data points for the experimental study represent the mean and range of results for 15 lumbar intervertebral disk specimens.

moments of 7.5 N·m, the range of motion in flexion–extension, axial rotation and lateral bending were 39 deg, 16 deg, and 28 deg, respectively. The flexion response was more flexible than the extension response, which is consistent with experimental observations. Excellent agreement was observed between the finite element model and experimental data for intradiscal pressure under pure compressive loading. The predicted facet joint forces were lower than those of experimental results and validated finite element models for extension and torsion, likely due to the nondegenerate properties chosen for the intervertebral disks and morphology of the young female spine. Overall, the presented finite model was in close agreement with the lumbar experiment studies and published state of the art finite element models. This work is the first of its kind to validate a computational lumbar spine model of a living 20-yr-old female subject. Furthermore, this model will serve as a valuable tool for predicting orthopedic spinal injuries, studying the effect of intervertebral disk replacements using advanced biomaterials, and investigating soft tissue degeneration in future work.

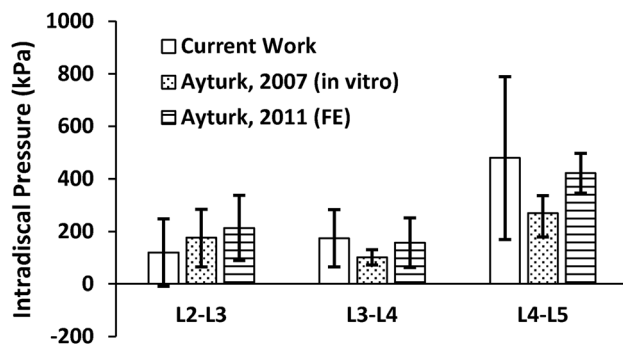


Fig. 13 IDP within L2–L3, L3–L4, and L4–L5 nuclei pulposi for flexion compared with experimental data [25] and a validated finite element model [18]. The L2–L3 and L3–L4 values correspond to an applied moment of 3.0 N·m, whereas the L4–L5 values correspond to an applied moment of 7.5 N·m. The first bar indicates the mean hydrostatic pressure and standard deviation within the nucleus pulposus for this work. The second bar corresponds to the mean measurement and standard deviation from the in vitro experimental study by Ayturk. The third bar corresponds to the mean IDP and standard deviation within the nucleus pulposus for a validated finite element model.

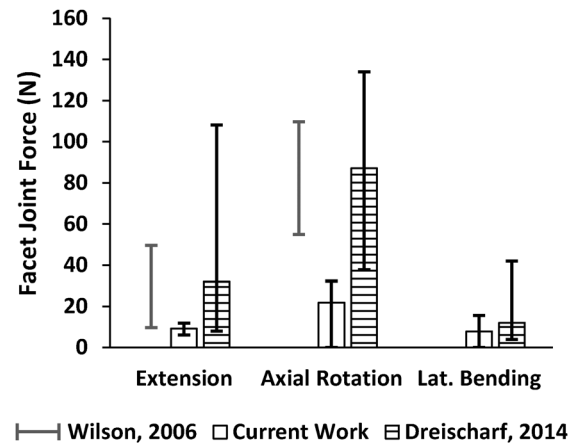


Fig. 14 Median FJFs of all spinal levels for extension, axial rotation, and lateral bending under applied moments of 7.5 N·m compared with experimental data [59] and validated finite element models [1]. The range given for this work corresponds to maximum and minimum FJFs in the model. The range indicated by the gray error bars represents the range of experimental results. The striped bar indicates the median FJF and range of results of eight validated finite element models.

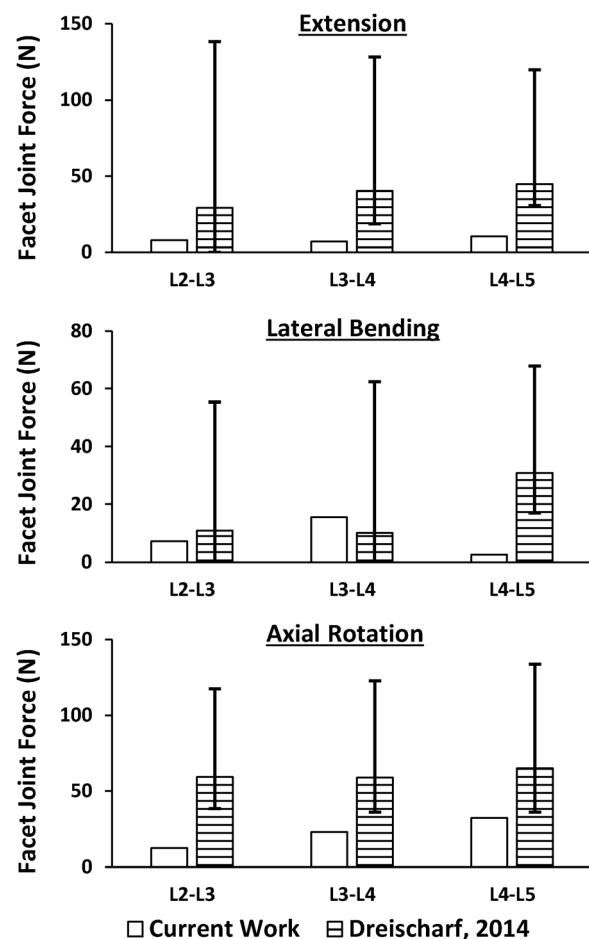


Fig. 15 FJFs at the L2–L3, L3–L4, and L4–L5 levels for extension (upper), lateral bending (middle), and axial rotation (lower) compared with validated finite element models [1]. The striped bar indicates the median FJF and range of results of eight validated finite element models.

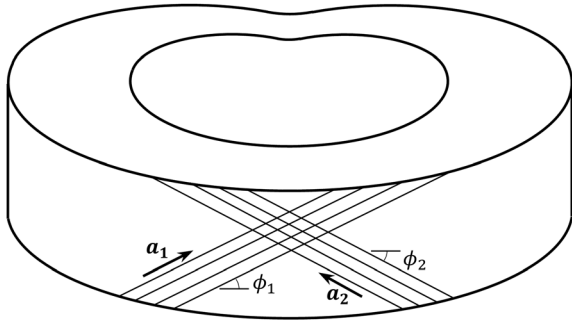


Fig. 16 Direction unit vectors for both fiber populations: \mathbf{a}_i —unit vector in direction of i th fiber population, ϕ_i —inclination of i th fiber population relative to horizontal

Funding Data

This work was funded by the DynaaTECC (Dynamics, acoustics, aeroelasticity, Theory, Experiments, Computations and Controls) Research Lab.

Nomenclature

a = anterior part of the vertebral body
 A = semi-major axis of ellipse
 $\mathbf{a}_1, \mathbf{a}_2$ = unit vectors of the fiber populations
 $\mathbf{A}_1, \mathbf{A}_2$ = tensors that account of the fiber orientation
 AF = annulus fibrosus
 ALL = anterior longitudinal ligament
 B = semiminor axis of ellipse
 \mathbf{C} = right Cauchy–Green deformation tensor
 $\bar{\mathbf{C}}$ = modified right Cauchy–Green deformation
 C_{10}, C_{01} = Mooney–Rivlin material model constants
 CT = computed tomography
 E_{ii} = Young's modulus in the i -direction
 f = vertebral foramen
 \mathbf{F} = deformation gradient
 F_i = initial load–displacement function of i th active ligament
 $F_{\text{new},i}$ = adjusted ligament load–displacement function of i th active ligament
 FCL = facet capsular ligament
 FE = finite element
 FEA = finite element analysis
 FJF = facet joint forces
 G_{ij} = shear modulus in j -direction with surface normal in the j -direction
 \bar{I}_1, \bar{I}_2 = first and second invariants of the modified right Cauchy–Green deformation tensor
 \bar{I}_1^*, \bar{I}_2^* = pseudo invariants of the modified right Cauchy–Green deformation tensor
 IDP = intradiscal pressure
 ISL = interspinous ligament
 ITL = intertransverse ligament
 J = volume ratio
 K = ligament force scaling factor
 k_1, k_2 = material properties of the fibers
 l = left pedicle
 $L2$ = second lumbar vertebra
 $L3$ = third lumbar vertebra
 $L4$ = fourth lumbar vertebra
 $L5$ = fifth lumbar vertebra
 LF = ligamentum flavum
 m = number of active ligaments
 M = moment
 n = number of data points
 NP = nucleus pulposus
 PLL = posterior longitudinal ligament

r = right pedicle
 RMSE = root-mean-square error for range of motion
 ROM = range of motion
 S = sacrum
 \mathbf{S} = second Piola–Kirchhoff stress tensor
 SSL = supraspinous ligament
 U = dilatational strain energy
 x = Cartesian coordinate in the lateral direction or ligament displacement
 \mathbf{X} = global coordinate system anterior direction
 \mathbf{x}_{L3} = L3 vertebra local coordinate system x -axis
 y = Cartesian coordinate in the anterior/posterior direction
 \mathbf{Y} = global coordinate system inferior direction
 \mathbf{y}_{L3} = L3 vertebra local coordinate system y -axis
 z = Cartesian coordinate in the superior/inferior direction
 \mathbf{Z} = global coordinate system transverse direction
 \mathbf{z}_{L3} = L3 vertebra local coordinate system z -axis

Greek Symbols

β = threshold value for root-mean-square error
 θ_{exp} = range of motion from experimental in vitro study
 θ_{sim} = range of motion computed through finite element simulation
 κ = bulk modulus
 ν_{ij} = Poisson's ratio corresponding to a contraction in the j -direction for a given extension in the i -direction
 σ_a = standard deviation of the Gaussian function that is centered at the anterior region of vertebral body
 σ_f = standard deviation of the Gaussian function that is centered at the vertebral foramen
 σ_l = standard deviation of the Gaussian function that is centered at the left pedicle
 σ_r = standard deviation of the Gaussian function that is centered at the right pedicle
 ϕ_1, ϕ_2 = inclination of fiber populations relative to horizontal
 ϕ_a = angular position that the Gaussian function that is centered at the anterior region of vertebral body
 ϕ_f = angular position that the Gaussian function that is centered at the vertebral foramen
 ϕ_l = angular position that the Gaussian function that is centered at the left pedicle
 ϕ_r = angular position that the Gaussian function that is centered at the right pedicle
 Ψ = Helmholtz free-energy function
 $\bar{\Psi}$ = distortional strain energy
 $\bar{\Psi}_f$ = distortional strain energy of the annulus fibrosus fibers
 $\bar{\Psi}_{\text{gs}}$ = distortional strain energy of the annulus fibrosus ground substance

Superscripts or Superscripts

a = anterior region of vertebral body
 exp = experimental
 f = fiber or vertebral foramen
 gs = ground substance
 i = Cartesian direction x, y , or z
 j = Cartesian direction x, y , or z
 l = left pedicle
 r = right pedicle
 sim = simulation

Appendix: Constitutive Equations

Soft biological tissues are often modeled using hyperelastic constitutive theories given their elastic behavior at large strains [45]. A compressible hyperelastic constitutive model has the general form

$$\mathbf{S} = 2 \frac{\partial \Psi(\mathbf{C})}{\partial \mathbf{C}} \quad (\text{A1})$$

where \mathbf{S} is the *second Piola–Kirchhoff stress tensor*, \mathbf{C} is the *right Cauchy–Green deformation tensor*, and Ψ is the *Helmholtz free-energy function* [45]. The form of the Helmholtz free-energy function determines the type of hyperelastic constitutive model.

Compressible hyperelasticity is based on the right Cauchy–Green deformation tensor \mathbf{C} given by

$$\mathbf{C} = \mathbf{F}^T \mathbf{F} \quad (\text{A2})$$

and its decomposition into distortional and dilatational components; namely

$$\mathbf{C} = J^{2/3} \bar{\mathbf{C}} \quad (\text{A3})$$

where \mathbf{F} is the deformation gradient, $\bar{\mathbf{C}}$ is the modified right Cauchy–Green deformation tensor, and J is the volume ratio (or Jacobian determinant).

Nucleus Pulposus. The Mooney–Rivlin model was used to represent the behavior of the nucleus pulposus given its isotropy and incompressibility under physiological loads [60]. This model is a simplification of the more general *Ogden model* for incompressible materials [45] and takes the form

$$\Psi(\mathbf{C}) = U(J) + \bar{\Psi}(\bar{\mathbf{C}}) \quad (\text{A4})$$

The dilatational strain energy $U(J)$ is given by

$$U(J) = \frac{\kappa}{2} (J - 1)^2 \quad (\text{A5})$$

where κ is the bulk modulus of the material. Due to the assumption of incompressibility, κ serves as a penalty parameter selected by the modeler [7]. The distortional strain energy $\bar{\Psi}(\bar{\mathbf{C}})$ is given by

$$\bar{\Psi}(\bar{\mathbf{C}}) = C_{10}(\bar{I}_1 - 3) + C_{01}(\bar{I}_2 - 3) \quad (\text{A6})$$

where C_{10} and C_{01} are constants related to the *shear modulus* in the reference configuration, and \bar{I}_1 and \bar{I}_2 are the first and second invariants of the modified right Cauchy–Green deformation tensor.

A.1.2 Annulus Fibrosus. For the annulus fibrosus, it was assumed that two fibers populations were embedded in an incompressible, isotropic ground substance. Therefore, the Helmholtz free-energy function takes the form

$$\Psi(\mathbf{C}) = U(J) + \bar{\Psi}_{\text{gs}}(\bar{\mathbf{C}}) + \bar{\Psi}_f(\bar{\mathbf{C}}, \mathbf{A}_1, \mathbf{A}_2) \quad (\text{A7})$$

where $\bar{\Psi}_{\text{gs}}$ and $\bar{\Psi}_f$ are the distortional strain energies of the ground substance and fibers, respectively.

A *Neo-Hookean model*, which is another simplification of the Ogden model, was used for the ground substance; namely

$$\bar{\Psi}_{\text{gs}}(\bar{\mathbf{C}}) = C_{10}(\bar{I}_1 - 3) \quad (\text{A8})$$

Due to the exponential stiffening of the AF observed experimentally [47], the following exponential strain energy function was used to model the two fiber populations [46]

$$\bar{\Psi}_f(\bar{\mathbf{C}}, \mathbf{A}_1, \mathbf{A}_2) = \frac{k_1}{2k_2} \left[e^{k_2(\bar{I}_1 - 1)^2} + e^{k_2(\bar{I}_2 - 1)^2} - 2 \right] \quad (\text{A9})$$

where \mathbf{A}_1 and \mathbf{A}_2 are tensors that account of the fiber orientation and are defined using the dyadic product as

$$\mathbf{A}_i = \mathbf{a}_i \otimes \mathbf{a}_i, \quad i = 1, 2 \quad (\text{A10})$$

with \mathbf{a}_i being the fiber direction unit vector determined by ϕ_i as depicted in Fig. 16. The pseudo invariants in Eq. (A9), \bar{I}_1^* and \bar{I}_2^* , are defined as

$$\bar{I}_i^* = \bar{\mathbf{C}} : \mathbf{A}_i, \quad i = 1, 2 \quad (\text{A11})$$

Finally, k_1 and k_2 are material properties of the fibers that are determined from fitting the above constitutive model to uniaxial stress–strain data of single lamellar samples [61]. Note that same equation for dilatational strain energy $U(J)$ given for the NP in Eq. (A5) was used for the AF, and is used solely for enforcing incompressibility.

References

- [1] Dreischarf, M., Zander, T., Shirazi-Adl, A., Puttlitz, C. M., Adam, C. J., Chen, C. S., Goel, V. K., Kiapour, A., Kim, Y. H., Labus, K. M., Little, J. P., Park, W. M., Wang, Y. H., Wilke, H. J., Rohlmann, A., and Schmidt, H., 2014, “Comparison of Eight Published Static Finite Element Models of the Intact Lumbar Spine: Predictive Power of Models Improves When Combined Together,” *J. Biomech.*, **47**(8), pp. 1757–1766.
- [2] Rohlmann, A., Zander, T., Schmidt, H., Wilke, H. J., and Bergmann, G., 2006, “Analysis of the Influence of Disc Degeneration on the Mechanical Behaviour of a Lumbar Motion Segment Using the Finite Element Method,” *J. Biomech.*, **39**(13), pp. 2484–2490.
- [3] Lipscomb, K. E., Sarigul-Klijn, N., Klineberg, E., and Mohan, V., 2017, “Biomechanical Effects of Human Lumbar Discography: In Vitro Experiments and Their Finite Element Validation,” *J. Clin. Spine Surg.*, **30**(3), pp. E219–E225.
- [4] Schmidt, H., Galbusera, F., Rohlmann, A., Zander, T., and Wilke, H.-J., 2012, “Effect of Multilevel Lumbar Disc Arthroplasty on Spine Kinematics and Facet Joint Loads in Flexion and Extension: A Finite Element Analysis,” *Eur. Spine J.*, **21**(S5), pp. 663–674.
- [5] Lin, H.-M., Pan, Y.-N., Liu, C.-L., Huang, L.-Y., Huang, C.-H., and Chen, C.-S., 2013, “Biomechanical Comparison of the K-ROD and Dynesys Dynamic Spinal Fixator Systems—A Finite Element Analysis,” *Bio-Med. Mater. Eng.*, **23**(6), p. 495.
- [6] Jones, A. C., and Wilcox, R. K., 2008, “Finite Element Analysis of the Spine: Towards a Framework of Verification, Validation and Sensitivity Analysis,” *Med. Eng. Phys.*, **30**(10), pp. 1287–1304.
- [7] Eberlein, R., Holzappel, G. A., and Fröhlich, M., 2004, “Multi-Segment FEA of the Human Lumbar Spine Including the Heterogeneity of the Annulus Fibrosus,” *Comput. Mech.*, **34**(2), pp. 147–163.
- [8] Breaux, C., Shirazi-Adl, A., and Guise, J., 1991, “Reconstruction of a Human Ligamentous Lumbar Spine Using CT Images—A Three-Dimensional Finite Element Mesh Generation,” *Ann. Biomed. Eng.*, **19**(3), pp. 291–302.
- [9] Shirazi-Adl, A., 1994, “Nonlinear Stress Analysis of the Whole Lumbar Spine in Torsion—Mechanics of Facet Articulation,” *J. Biomech.*, **27**(3), p. 289293.
- [10] Shirazi-Adl, A., 1994, “Biomechanics of the Lumbar Spine in Sagittal/Lateral Moments,” *Spine*, **19**(21), pp. 2407–2414.
- [11] Kong, W. Z., Goel, V. K., and Gilbertson, L. G., 1998, “Prediction of Biomechanical Parameters in the Lumbar Spine During Static Sagittal Plane Lifting,” *ASME J. Biomech. Eng.*, **120**(2), pp. 273–280.
- [12] Chen, C.-S., Cheng, C.-K., Liu, C.-L., and Lo, W.-H., 2001, “Stress Analysis of the Disc Adjacent to Interbody Fusion in Lumbar Spine,” *Med. Eng. Phys.*, **23**(7), pp. 485–493.
- [13] Chen, C.-S., Cheng, C.-K., and Liu, C.-L., 2002, “A Biomechanical Comparison of Posterolateral Fusion and Posterior Fusion in the Lumbar Spine,” *J. Spinal Disord. Tech.*, **15**(1), pp. 53–63.
- [14] Zander, T., Rohlmann, A., Calisse, J., and Bergmann, G., 2001, “Estimation of Muscle Forces in the Lumbar Spine During Upper-Body Inclination,” *Clin. Biomech.*, **16**, pp. S73–S80.
- [15] Zander, T., Rohlmann, A., Klöckner, C., and Bergmann, G., 2002, “Comparison of the Mechanical Behavior of the Lumbar Spine Following Mono- and Bisegmental Stabilization,” *Clin. Biomech.*, **17**(6), pp. 439–445.
- [16] Little, J. P., De Visser, H., Pearcy, M. J., and Adam, C. J., 2008, “Are Coupled Rotations in the Lumbar Spine Largely Due to the Osseous-Ligamentous Anatomy?—A Modeling Study,” *Comput. Methods Biomech. Biomed. Eng.*, **11**(1), pp. 95–103.
- [17] Zander, T., Rohlmann, A., and Bergmann, G., 2009, “Influence of Different Artificial Disc Kinematics on Spine Biomechanics,” *Clin. Biomech.*, **24**(2), pp. 135–142.
- [18] Ayturk, U. M., and Puttlitz, C. M., 2011, “Parametric Convergence Sensitivity and Validation of a Finite Element Model of the Human Lumbar Spine,” *Comput. Methods Biomech. Biomed. Eng.*, **14**(8), pp. 695–705.
- [19] Liu, C.-L., Zhong, Z.-C., Hsu, H.-W., Shih, S.-L., Wang, S.-T., Hung, C., and Chen, C.-S., 2011, “Effect of the Cord Pretension of the Dynesys Dynamic Stabilisation System on the Biomechanics of the Lumbar Spine: A Finite Element Analysis,” *Eur. Spine J.*, **20**(11), pp. 1850–1858.
- [20] Kiapour, W. A., Ambati, K. D., Hoy, K. R., and Goel, K. V., 2012, “Effect of Graded Facetectomy on Biomechanics of Dynesys Dynamic Stabilization System,” *Spine*, **37**(10), pp. E581–E589.
- [21] Park, W. M., Kim, K., and Kim, Y. H., 2013, “Effects of Degenerated Intervertebral Discs on Intersegmental Rotations, Intradiscal Pressures, and Facet

- Joint Forces of the Whole Lumbar Spine," *Comput. Biol. Med.*, **43**(9), pp. 1234–1240.
- [22] Xu, M., Yang, J., Lieberman, I. H., and Haddas, R., 2017, "Lumbar Spine Finite Element Model for Healthy Subjects: Development and Validation," *Comput. Methods Biomech. Biomed. Eng.*, **20**(1), pp. 1–15.
- [23] Ackerman, M. J., 1998, "The Visible Human Project," *Proc. IEEE*, **86**(3), pp. 504–511.
- [24] Schmidt, H., Heuer, F., Simon, U., Kettler, A., Rohlmann, A., Claes, L., and Wilke, H. J., 2006, "Application of a New Calibration Method for a Three-Dimensional Finite Element Model of a Human Lumbar Annulus Fibrosus," *Clin. Biomech. (Bristol, Avon)*, **21**(4), pp. 337–344.
- [25] Ayturk, U. M., 2007, "Development and Validation of a Three Dimensional High Resolution Nonlinear Finite Element Model of an L3/L4 Functional Spinal Unit," Master's thesis, Colorado State University, Fort Collins, CO.
- [26] van der Houwen, E. B., Baron, P., Veldhuizen, A. G., Burgerhof, J. G., van Ooijen, P. M., and Verkerke, G. J., 2010, "Geometry of the Intervertebral Volume and Vertebral Endplates of the Human Spine," *Ann. Biomed. Eng.*, **38**(1), pp. 33–40.
- [27] Tang, R., Gungor, C., Sesek, R. F., Foreman, K. B., Gallagher, S., and Davis, G. A., 2016, "Morphometry of the Lower Lumbar Intervertebral Discs and Endplates: Comparative Analyses of New MRI Data With Previous Findings," *Eur. Spine J.*, **25**(12), pp. 4116–4131.
- [28] Zhou, S. H., McCarthy, I. D., McGregor, A. H., Coombs, R. R. H., and Hughes, S. P. F., 2000, "Geometrical Dimensions of the Lower Lumbar Vertebrae—Analysis of Data From Digitised CT Images," *Eur. Spine J.*, **9**(3), pp. 242–248.
- [29] Bailey, J. F., Sparrey, C. J., Been, E., and Kramer, P. A., 2016, "Morphological and Postural Sexual Dimorphism of the Lumbar Spine Facilitates Greater Lordosis in Females," *J. Anat.*, **229**(1), pp. 82–91.
- [30] Zander, T., Dreischarf, M., Timm, A.-K., Baumann, W. W., and Schmidt, H., 2017, "Impact of Material and Morphological Parameters on the Mechanical Response of the Lumbar Spine—A Finite Element Sensitivity Study," *J. Biomech.*, **53**, pp. 185–190.
- [31] Lipscomb, K. E., 2014, "Biomechanical Changes in the Whole Human Spine Due to Intervertebral Disc Degeneration and Fusion," University of California, Davis, CA.
- [32] Lipscomb, K., Sarigul-Klijn, N., and Klineberg, E. O., 2016, "Characterization of Lumbar-Level Spinal Fusion on the Whole Human Spine Under Vibrations," *ASME Paper No. IMECE2016-66384*.
- [33] Townsend, M. T., and Sarigul-Klijn, N., 2018, "Human Spaceflight and Space Adaptations: Computational Simulation of Gravitational Unloading on the Spine," *Acta Astronaut.*, **145**, pp. 18–27.
- [34] Townsend, M. T., and Sarigul-Klijn, N., 2016, "Updated Lagrangian Finite Element Formulations of Various Biological Soft Tissue Non-Linear Material Models: A Comprehensive Procedure and Review," *Comput. Methods Biomech. Biomed. Eng.*, **19**(11), pp. 1137–1142.
- [35] Lipscomb, K. E., and Sarigul-Klijn, N., "Simulation of the Whole Human Spine Using Finite Elements: P & H Version Convergence," *ASME Paper No. SBC2013-14298*.
- [36] Heuer, F., Schmidt, H., Klezl, Z., Claes, L., and Wilke, H.-J., 2007, "Stepwise Reduction of Functional Spinal Structures Increase Range of Motion and Change Lordosis Angle," *J. Biomech.*, **40**(2), pp. 271–280.
- [37] Schmidt, H., Heuer, F., Drumm, J., Klezl, Z., Claes, L., and Wilke, H.-J., 2007, "Application of a Calibration Method Provides More Realistic Results for a Finite Element Model of a Lumbar Spinal Segment," *Clin. Biomech. (Bristol, Avon)*, **22**(4), p. 377.
- [38] Guo, L.-X., and Teo, E.-C., 2006, "Influence Prediction of Injury and Vibration on Adjacent Components of Spine Using Finite Element Methods," *J. Spin. Disord. Tech.*, **19**(2), pp. 118–124.
- [39] Lu, M. Y., Hutton, C. W., and Gharpuray, M. V., 1996, "Do Bending, Twisting, and Diurnal Fluid Changes in the Disc Affect the Propensity to Prolapse? A Viscoelastic Finite Element Model," *Spine*, **21**(22), pp. 2570–2579.
- [40] Rho, J. Y., Hobatho, M. C., and Ashman, R. B., 1995, "Relations of Mechanical Properties to Density and CT Numbers in Human Bone," *Med. Eng. Phys.*, **17**(5), pp. 347–355.
- [41] Shirazi-Adl, M. A., Ahmed, C. A., and Shrivastava, C. S., 1986, "Mechanical Response of a Lumbar Motion Segment in Axial Torque Alone and Combined With Compression," *Spine*, **11**(9), pp. 914–927.
- [42] Thomas Edwards, A. W., Zheng, A. Y., Ferrara, A. L., and Yuan, A. H., 2001, "Structural Features and Thickness of the Vertebral Cortex in the Thoracolumbar Spine," *Spine*, **26**(2), pp. 218–225.
- [43] Woldtvedt, D. J., Womack, W., Gadowski, B. C., Schuldt, D., and Puttlitz, C. M., 2011, "Finite Element Lumbar Spine Facet Contact Parameter Predictions Are Affected by the Cartilage Thickness Distribution and Initial Joint Gap Size," *ASME J. Biomech. Eng.*, **133**(6), p. 061009.
- [44] Dassault Systèmes Simulia Corp., 2014, "Contact Formulations and Numerical Methods," *Abaqus Analysis User's Guide* (6.14), Dassault Systèmes Simulia Corp, Providence, RI.
- [45] Holzapfel, G. A., 2000, *Nonlinear Solid Mechanics: A Continuum Approach for Engineering*, Wiley, Chichester, NY.
- [46] Spencer, A. J. M., 1972, *Deformations of Fibre-Reinforced Materials*, Clarendon Press, Oxford, UK.
- [47] Holzapfel, G. A., Schulze-Bauer, C. A., Feigl, G., and Regitnig, P., 2005, "Single Lamellar Mechanics of the Human Lumbar Anulus Fibrosus," *Bio-mech. Model. Mechanobiol.*, **3**(3), pp. 125–140.
- [48] Dreischarf, M., Zander, T., Bergmann, G., and Rohlmann, A., 2010, "A Non-Optimized Follower Load Path May Cause Considerable Intervertebral Rotations," *J. Biomech.*, **43**(13), pp. 2625–2628.
- [49] Korez, R., Likar, B., Pernus, F., and Vrtovec, T., 2014, "Parametric Modeling of the Intervertebral Disc Space in 3D: Application to CT Images of the Lumbar Spine," *Comput. Med. Imaging Graph.*, **38**(7), pp. 596–605.
- [50] Wilke, H. J., Wenger, K., and Claes, L., 1998, "Testing Criteria for Spinal Implants: Recommendations for the Standardization of In Vitro Stability Testing of Spinal Implants," *Eur. Spine J.*, **7**(2), pp. 148–154.
- [51] Maas, S. A., Ellis, B. J., Rawlins, D. S., and Weiss, J. A., 2016, "Finite Element Simulation of Articular Contact Mechanics With Quadratic Tetrahedral Elements," *J. Biomech.*, **49**(5), pp. 659–667.
- [52] Rohlmann, A., Neller, S., Claes, L., Bergmann, G., and Wilke, H.-J., 2001, "Influence of a Follower Load on Intradiscal Pressure and Intersegmental Rotation of the Lumbar Spine," *Spine*, **26**(24), pp. E557–E561.
- [53] White, A. A. P., and Manohar, M., 1978, *Clinical Biomechanics of the Spine*, Lippincott, Philadelphia, PA.
- [54] Panjabi, M. M., Oxland, R. T., Yamamoto, J. I., and Crisco, J. J., 1994, "Mechanical Behavior of the Human Lumbar and Lumbosacral Spine as Shown by Three-Dimensional Load-Displacement Curves," *J. Bone Jt. Surg.*, **76**(3), pp. 413–424.
- [55] Brinckmann, P., and Grootenboer, H., 1991, "Change of Disc Height, Radial Disc Bulge, and Intradiscal Pressure From Discectomy an In Vivo Investigation on Human Lumbar Discs," *Spine*, **16**(6), pp. 641–646.
- [56] Shan, Z., Li, S., Liu, J., Mamuti, M., Wang, C., and Zhao, F., 2015, "Correlation Between Biomechanical Properties of the Annulus Fibrosus and Magnetic Resonance Imaging (MRI) Findings," *Eur. Spine J.*, **24**(9), pp. 1909–1916.
- [57] O'Connell, G., Sen, S., and Elliott, D., 2012, "Human Annulus Fibrosus Material Properties From Biaxial Testing and Constitutive Modeling Are Altered With Degeneration," *Mech. Model. Mechanobiol.*, **11**(3), pp. 493–503.
- [58] Skrzypiec, A. D., Tarala, A. M., Pollintine, A. P., Dolan, A. P., and Adams, A. M., 2007, "When Are Intervertebral Discs Stronger Than Their Adjacent Vertebrae?," *Spine*, **32**(22), pp. 2455–2461.
- [59] Wilson, D. C., Niosi, C. A., Zhu, Q. A., Oxland, T. R., and Wilson, D. R., 2006, "Accuracy and Repeatability of a New Method for Measuring Facet Loads in the Lumbar Spine," *J. Biomech.*, **39**(2), p. 348.
- [60] Bachrach, N. M., Mow, V. C., and Guilak, F., 1998, "Incompressibility of the Solid Matrix of Articular Cartilage Under High Hydrostatic Pressures," *J. Biomech.*, **31**(5), pp. 445–451.
- [61] Eberlein, R., Holzapfel, G. A., and Schulze-Bauer, C. A. J., 2001, "An Anisotropic Model for Annulus Tissue and Enhanced Finite Element Analyses of Intact Lumbar Disc Bodies," *Comput. Methods Biomech. Biomed. Eng.*, **4**(3), pp. 209–229.